Regulation of energy and mass transport in a hydrogen-bonded framework for visible-light-driven CO_2 reduction in water

Jiaxing Xu,[†,§] Xiang Zhang,[†,§] Lijuan Ma,[†] Tao Wu,[†] Hui Wang,[†] Yuanfang Deng,[†] Jun Xia,[†] Zhongyang Qiu,[†] Kai Sun,[†] Aiyong He,[†] Jian Zhang,[‡,*] Xu Zhang[‡,*] and Banglin Chen[∥]

[†]Jiangsu Key Laboratory for Biomass-Based Energy and Enzyme Technology, School of Chemistry and Chemical Engineering, Huaiyin Normal University, Huaian 223300, China;

[‡]The Molecular Foundry, Lawrence Berkeley National Laboratory, Berkeley, California 94720, United States;

[∥]Fujian Provincial Key Laboratory of Polymer Materials, College of Chemistry and Materials, Fujian Normal University, Fuzhou 350007, China; Key Laboratory of the Ministry of Education for Advanced Catalysis Materials, College of Chemistry and Materials Science, Zhejiang Normal University, Jinhua 321004, China.

ABSTRACT: Photoenzymatic reduction of CO_2 to formate is a promising strategy for carbon valorization, yet its efficiency is still limited by inefficient energy and mass transport. Here, we design a series of isostructural hydrogen-bonded organic frameworks (HOFs) that establish confinement effects to promote photocatalytic NADH regeneration and the subsequent NADH-dependent enzymatic CO_2-to-formate reduction. We demonstrate that spatial confinement within the framework channels localizes exciton migration to nanoscale domains and promotes interfacial dissociation. Additionally, Rh-induced electronic-structure modulation enables ultrafast electron transfer, while the intrinsic hydrogen-bond network furnishes directional proton conduction to NAD^+. These synergistic regulations afford a photocatalytic NADH regeneration efficiency of 99.8% with a record apparent quantum efficiency of 32.8%, and drive formate production at a rate of 3020 μmol g^{-1} h^{-1} with 100% selectivity—the highest rate reported to date for all light-driven systems in water. The HOF-based catalyst retains 86.3% of its initial activity over five cycles, highlighting its robustness. This work offers mechanistic insight into how microenvironment engineering within HOF architectures regulates energy and mass transport in photoenzymatic catalysis, paving the way for the rational design of advanced hybrid catalytic systems.

INTRODUCTION

Amid the restructuring of the global energy system, the direct solar conversion of CO_2 into storable chemicals and fuels has become a central frontier in materials science and photochemistry.[1] Formic acid, serving both as a liquid hydrogen carrier and a versatile C_1 platform, stands out as a particularly attractive target.[2] Achieving CO_2-to-formate reduction under mild conditions offers a unified solution to renewable chemical synthesis and carbon-neutral strategies. To this end, direct photocatalytic CO_2 reduction has been extensively explored in semiconductors,[3,4] metal-organic frameworks (MOFs),[5,6] covalent organic frameworks (COFs),[7,8] and other hybrid materials,[9,10] yielding notable advancements. However, current CO_2-to-formate photocatalysis generally relies on organic solvents,[11,12] and visible-light operation in water remains scarce, significantly limiting prospects for green and sustainable applications. Moreover, suboptimal spatiotemporal coupling among exciton diffusion, electron-proton transfer, and molecular transport in photocatalysis prevents efficient routing of energy and mass into the formate pathway,[13] thereby depressing selectivity and conversion.

Natural photosynthesis offers a model for addressing these limitations. In nature, chloroplasts achieve remarkable energy conversion efficiency in aqueous environments through highly organized nanoscale architectures that coordinate exciton dissociation, electron–proton transport, and enzymatic cofactor shuttling.[14,15] Inspired by this, artificial photoenzymatic catalysis combines light-driven cofactor regeneration with selective enzymatic reduction, thereby overcoming the issues of enzymatic cofactor availability and photocatalytic selectivity. To surpass direct photocatalysis, photoenzymatic systems must tightly couple the two steps to confine energy and mass transport at the nanoscale. This goal requires a platform capable of orchestrating multichannel transport, directing excitonic energy, providing electron relays and low-barrier proton pathways, and integrating enzymes in aqueous conditions.

Crystalline porous frameworks, by virtue of ordered channels and designable sites, hold significant potential in photoenzymatic catalysis.[16-18] They can immobilize photosensitizers, enzymes, or cofactors (e.g., NAD^+/NADH), facilitate electron transfer, and integrate catalytic sites for solar-to-chemical energy conversion. Wang and coworkers demonstrated linkage-dependent photocatalytic NADH regeneration in conjugated COFs.[19] Liu and coworkers achieved NADH regeneration and CO_2-to-formate conversion using a MIL-125-NH_2 MOF with a covalently anchored Rh complex,[20] and the Ouyang group enhanced cofactor regeneration in triazine COFs via N-heterocyclic microenvironments.[21] Despite these advances, conventional frameworks face several constraints in aqueous photoenzymatic catalysis. First, in situ enzyme incorporation–favorable for interface compatibility–is often infeasible due to the harsh synthesis conditions of these frameworks. Second, the limited proton conductivity of most reported frameworks hampers coordinated electron–proton transfer, which is critical for NADH regeneration. Third, integrating multiple functional components increases design complexity, and research that holistically orchestrates multiple processes, such as exciton dissociation and electron transfer, remains scarce. By contrast, hydrogen-bonded organic frameworks (HOFs) exhibit a unique compatibility with the aforementioned requirements, yet remain scarcely explored.[22] Assembled through directional hydrogen bonding, HOFs can be formed in water in a single step, enabling in situ enzyme encapsulation under mild conditions. This bottom-up approach ensures high enzyme loading and structural integrity while maintaining crystalline pore accessibility.[23] Their intrinsic hydrogen-bond networks organize water into proton wires, and monomer diversity permits modular incorporation of photoactive ligands and electron-transfer relays.[24,25] Consequently, HOFs provide a distinct platform from traditional frameworks for orchestration of spatiotemporally coupled processes, including exciton dissociation, electron relays, proton delivery and enzyme recognition.

In this study, we propose and implement an HOF-based photoenzymatic catalytic strategy. Distinct from prior framework platforms, this system enables simple one-pot co-assembly in water of photoactive ligands, electron relays, and formate dehydrogenase (FDH). Moreover, the central design principle is to harness spatiotemporal confinement within HOFs to synergistically enhance excitonic, electronic, protonic and enzymatic pathways for formate production, thereby emulating the ordered light–chemical processes in chloroplast.[14] Time-resolved spectroscopy and first-principles calculation reveal that spatial confinement, electronic-structure modulation, and hydrogen-bond interaction cooperatively govern photogenerated-energy and mass transport within the HOF architecture. In the optimal HOF-2-Rh platform, we demonstrate that the interpenetrated microporous lattice restricts exciton diffusion to ~1.87 nm, and enables rapid dissociation, whereas Rh-induced confinement facilitates ultrafast electron transfer within ~0.85 ps. The extended hydrogen-bond network provides directional proton pathways via Grotthuss hopping and stabilizes NADH–enzyme interactions. Moreover, FDH is in situ encapsulated in HOF-2-Rh at ultrahigh loading while retaining its native catalytic activity. These synergistic effects deliver record yields of photocatalytic NADH regeneration and formate production in water.

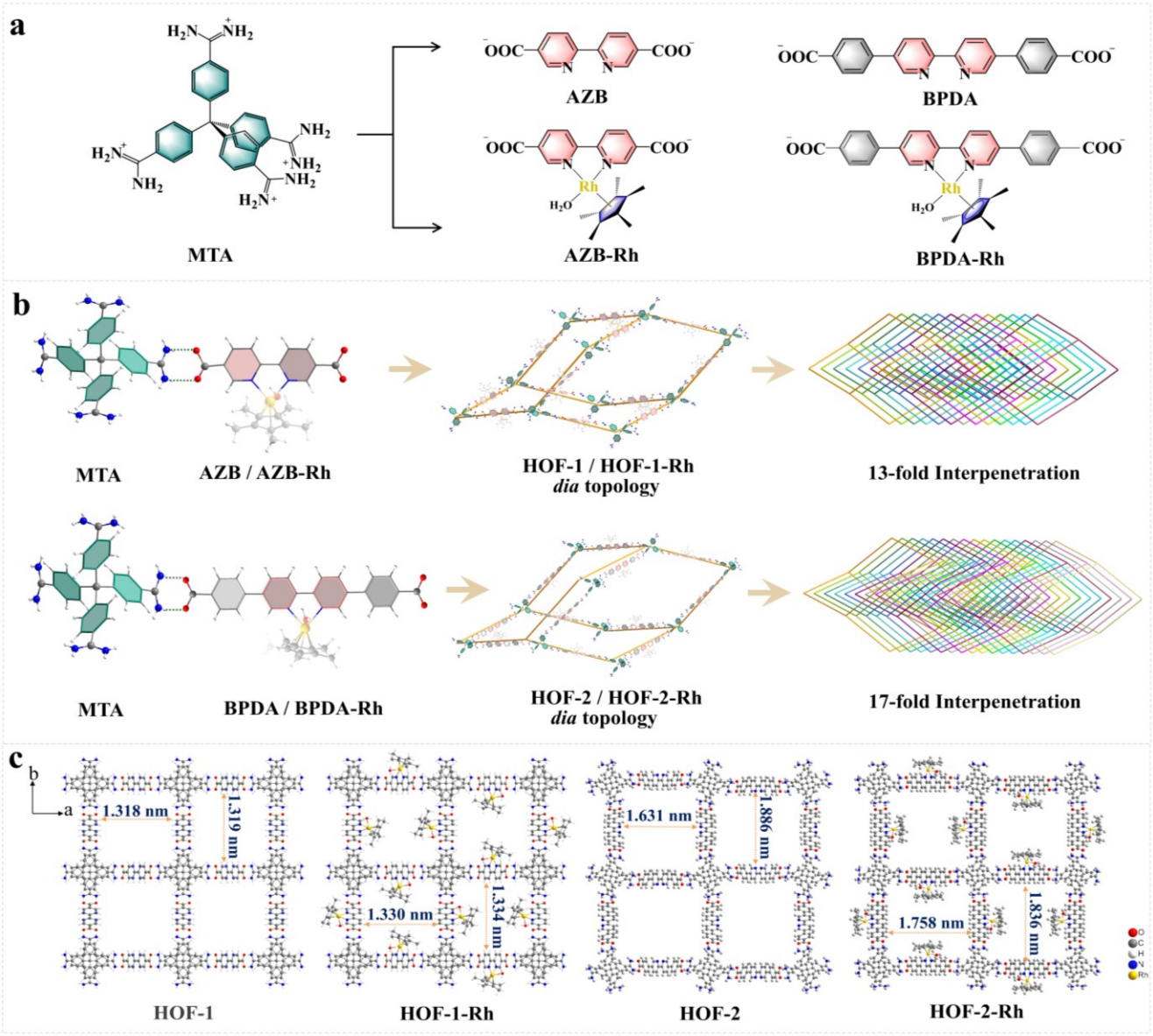

Figure 1. (a) The synthesis and structures of HOFs with different components designed to modulate the excited-state electronic structure and charge transport properties. Methanetetrayltetrakis(benzene-4,1-diyl) tetrakis (aminomethaniminium) (MTA); [2,2'-Bipyridine]-5,5'-dicarboxylic acid (AZB); 4,4'-([2,2'-bipyridine]-5,5'-diyl)dibenzoic acid (BPDA). (b). The *dia* topology and interpenetrated network of HOF-1/HOF-1-Rh and HOF-2/HOF-2-Rh formed by complementary double hydrogen-bonding interactions. (c) The stacking crystal structure of HOF observed along the c-axis.

RESULTS AND DISCUSSION

Structural Basis of Confinement Effect in HOFs. We employed an amidiniumcarboxylate bridge to construct HOFs, selecting a four-connected tetraamidinium tecton (Figure 1a) to link bipyridine-based dicarboxylate, forming interpenetrated diamondoid networks. Such close packing is expected to confine excitons within nanoscale domains, limit diffusion, and promote rapid interfacial dissociation. The bipyridine linkers also enable facile anchoring Cp^*Rh centers with tunable size and electronic properties. Aqueous self-assembly of these components yielded HOF-1, HOF-2, and their Rh-coordinated analogues (HOF-1-Rh, HOF-2-Rh). Single-crystal X-ray diffraction (SCXRD) confirmed that all frameworks adopt distorted diamondoid (*dia*) topologies with high interpenetr-

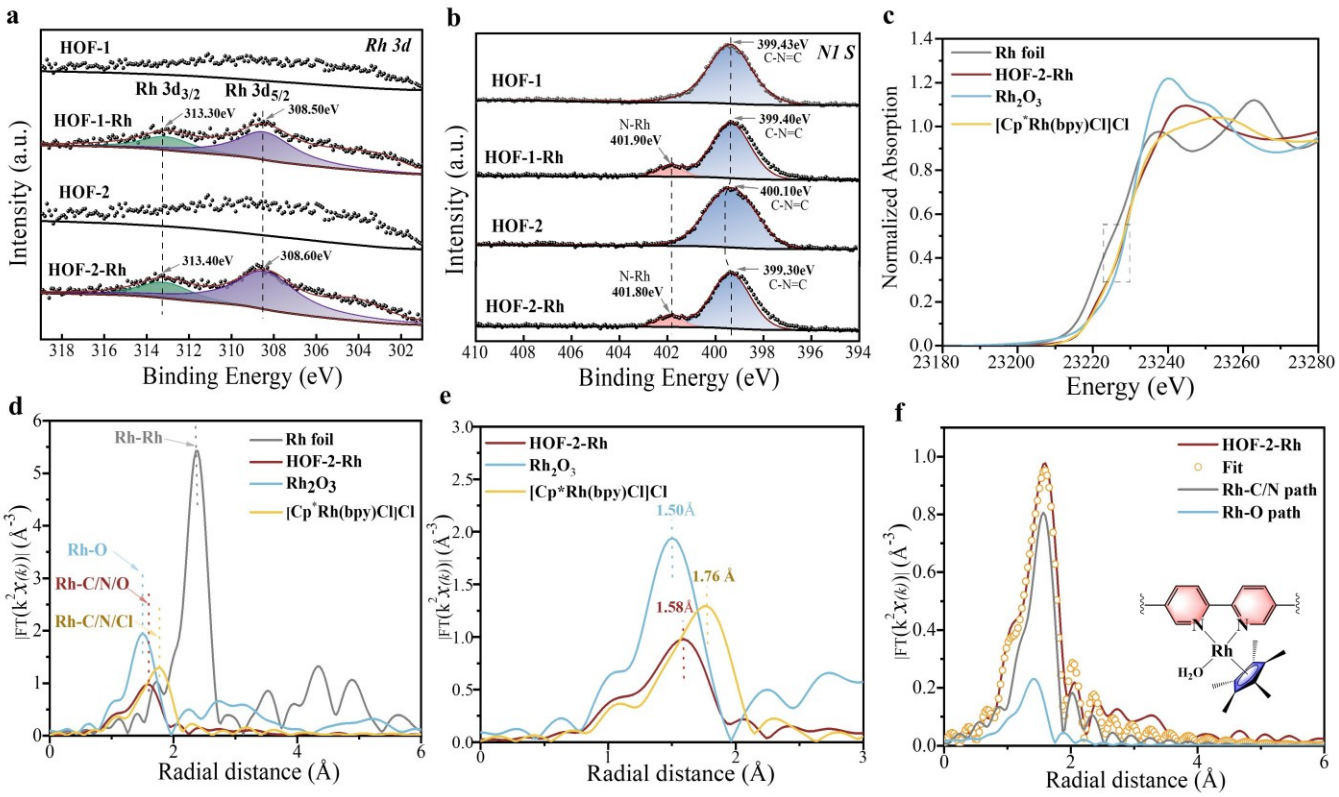

Figure 2. XPS spectra of (a) N 1s and (b) Rh 3d for pristine and Rh-coordinated HOFs. (c) Experimental Rh K-edge XANES spectra for Rh foil, Rh_2O_3, [Cp*Rh(bpy)Cl]Cl, and HOF-2-Rh. (d) Complete EXAFS spectra for the four samples. (e) Local EXAFS spectra showing the main peak positions of Rh for Rh_2O_3, [Cp*Rh(bpy)Cl]Cl, and HOF-2-Rh. (f) R-space fitting curve for HOF-2-Rh. The solid line represents experimental data, while the red dot line represents the best-fit curves.

ation (Figure 1b, Table S1). HOF-1 and HOF-1-Rh crystalize in $I4_1/amd$ and $I\bar{4}$ space groups, respectively, with 13-fold interpenetrated *dia* networks and uniform square channels of ~1.3 nm × 1.3 nm (Figure 1b, c), arising from shorter bipyridine linkers. In contrast, HOF-2 and HOF-2-Rh crystallize in $I\bar{4}_2d$ and $I\bar{4}$ space groups with 17-fold interpenetration, yielding slightly larger channels (~1.9 nm × 1.6 nm for HOF-2; ~1.8 nm × 1.7 nm for HOF-2-Rh) due to longer bipyridine linkers along the c-axis (Figure 1b, c). Probe-based calculations (1.82 Å) indicated higher porosities (58.5%, 47.1% vs. 48.0%, 29.8%) and larger Connolly surface areas (2496, 2625 vs. 2189, 2449 $m^2 g^{-1}$) for HOF-2/HOF-2-Rh compared to their HOF-1 analogues, suggesting enhanced molecular diffusion for enzyme substrates and cofactors.

All four HOFs are stabilized by complementary double hydrogen-bonds, forming amidinium–carboxylate synthons (N···O: 2.785(9)–2.902(14) Å; N–H···O: 163.3–177.7°; Figure S2,3), as supported by preserved FTIR signals for amidinium N–H (740 cm^{-1}) and carboxylate C=O (1687 cm^{-1}) (Figure S4). Broad O–H/N–H stretches (3100–3500 cm^{-1}) further indicate extended hydrogen-bond networks.[26] These highly interpenetrated frameworks exhibit exceptional stability under pH 2 and 12 (Figure S5,6; Table S2, 3), preserving confined microenvironments. Ordered channels generate nanoscale domains that could restrict exciton diffusion and promote localized dissociation, mitigating recombination losses common in large organic semiconductors.[27-30] Furthermore, >4 Å interlayer spacing forms vertically aligned pathways that could confine excitons in-plane, limiting out-of-plane delocalization (Figure S2,3). Confined within the micropores, the proton-conducting microenvironment arising from the intrinsic hydrogen-bond network could facilitate efficient proton transport.

Beyond crystallographic analysis, Rh incorporation was verified by ^{1}H NMR (Figure S7) and XPS, which showed Rh (III) $3d_{5/2}/3d_{3/2}$ doublets at 308/313 eV and a new N 1s peak (~401 eV), confirming Rh–N bond formation (Figure 2a,b).[31] Scanning electron microscopy (SEM) revealed filamentous morphologies (nanometer widths, micron lengths) across all frameworks (Figure S8), with Cp*Rh incorporation having minimal effect on size and shape. Energy-dispersive X-ray spectroscopy (EDS) mapping confirmed uniform Rh distribu-

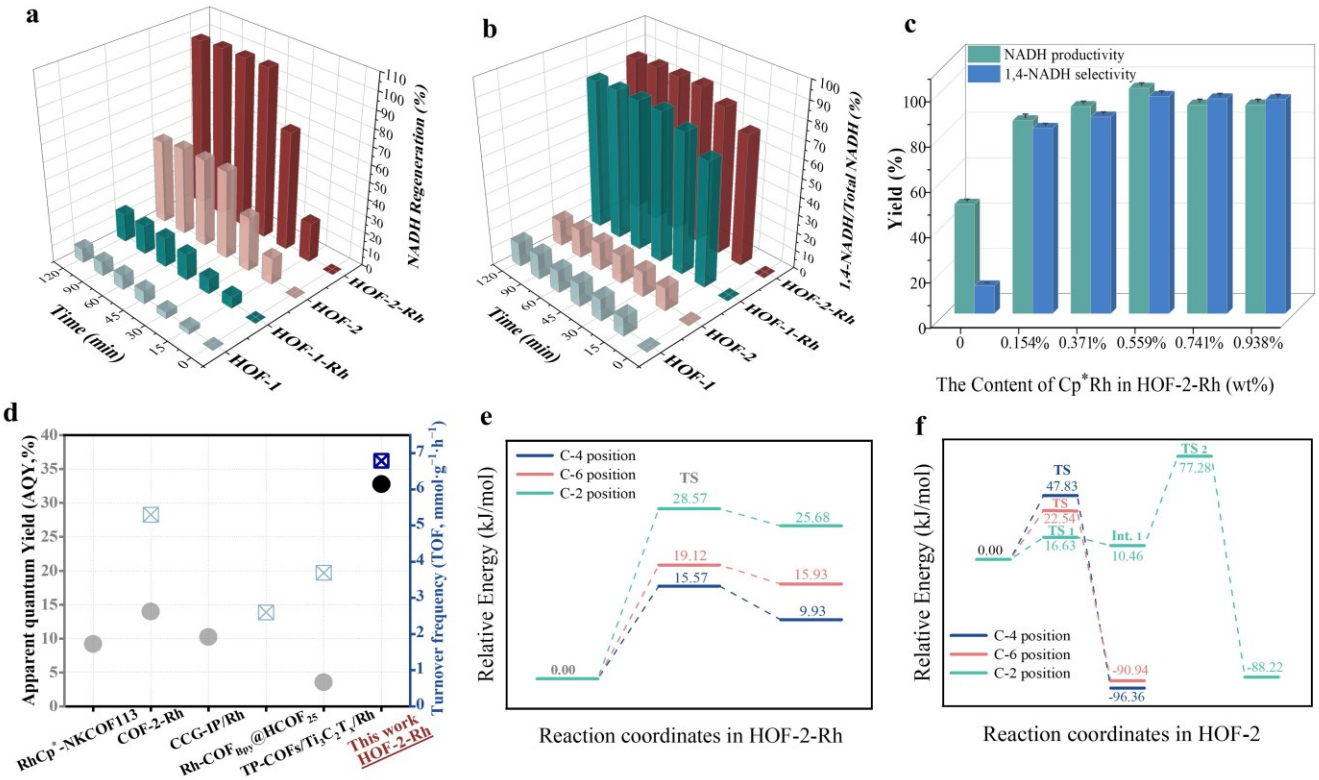

Figure 3. Photocatalytic NADH Regeneration Performance. Kinetics of photocatalytic total NADH (a) and bioactive 1,4-NADH (b) regeneration over HOF-1, HOF-1-Rh, HOF-2, and HOF-2-Rh. (c) Influence of Cp*Rh loading content in HOF-2-Rh on photocatalytic NADH regeneration efficiency and 1,4-NADH regioselectivity after 45 min irradiation. (d) Comparative photocatalytic performance of HOF-2-Rh and reported crystalline framework catalysts for NADH regeneration TOF and apparent quantum efficiency. Free energy profiles for regioselective hydride transfer from HOF-2-Rh (e) and HOF-2 (f) toward NAD^+ pyridine ring in the formation of 1,4-NADH, 1,6-NADH, and 1,2-NADH isomers.

tion in HOF-1-Rh and HOF-2-Rh (Figure S9). Enabling discreet, internal electron-accepting sites that couple with confined exciton dissociation to direct charge toward catalytic interfaces without compromising pore accessibility.

X-ray absorption fine structure (XAFS) analysis elucidated the Rh coordination environment in HOF-2-Rh (Figure S10). X-ray absorption near edge structure (XANES) spectra showed an edge shift relative to Rh foil and matched [Cp*Rh(bpy)Cl]Cl, confirming Rh (III) (Figure 2c). The absence of Rh-Rh scattering (~2.4 Å) in extended X-ray absorption fine structure (EXAFS) indicated atomically dispersed Rh species (Figure 2d, S11). The first-shell distance (1.58 Å) was closer to Rh_2O_3 (1.50 Å) than [Cp*Rh(bpy)Cl]Cl (1.76 Å), consistent with aqueous chloride-water exchange (Figure 2e), as supported by wavelet transform analysis (Figure S12). EXAFS fitting revealed 7.1 Rh-C/N and 1.0 Rh-O bonds (total CN = 8.1; Figure 2f, Table S4), in agreement with the Rh-C_5N_2O geometry from SCXRD (Table S1). This well-defined environment provides Cp*Rh centers with localized electronic fields that likely act as electron sinks, capturing and directing charge to catalytic sites. Overall, the engineered architectures couple spatial confinement from interpenetrated topologies, electronic modulation from Rh centers, and hydrogen-bond interactions intrinsic to HOFs.

Confinement-Engineered HOFs for Selective Photocatalytic NADH Regeneration. We probed whether the confinement effects of HOFs translate into enhanced photocatalysis by correlating NAD^+ reduction activity with optoelectronic properties. All variants exhibited sufficiently negative E_{CB} for NAD^+ reduction (Figure S13, 14).[32] HOF-2 delivered a 6.7-fold higher NADH yield than HOF-1 (52.2%; Figure 3a), owing to phenyl-conjugated linkers that red-shifted narrowed the band gap the absorption onset by 82 nm (337 → 419 nm; Figure S15) and (3.05 eV vs. 3.68 eV; Figure S16), boosting visible-light excitation. Despite this, regioselectivity for bioactive 1,4-NADH remained <16% for both, reflecting non-directional electron transfer in mediator-free systems (Figure 3b).[33,34] Cp*Rh coordination within framework channels markedly enhanced both yield and selectivity, reaching 81.7% (HOF-1-Rh) and 85.4% (HOF-2-Rh), likely via discrete Rh relay sites enabling directional hydride delivery. Rh

incorporation also induced further red shifts ($\Delta\lambda$ = 4 nm for HOF-1-Rh; 15 nm for HOF-2-Rh) (Figure S15), extending visible-light absorption. Optimal Rh loading (0.559 wt%, Table S5) in HOF-2-Rh afforded 99.8% NAD^+ conversion with 95.3% 1,4-NADH selectivity (Figure 3c), an AQY of 32.8% at 420 nm, and a TOF of 6.79 mmol g^{-1} h^{-1} (Figure 3d), surpassing all reported framework platforms (Table S6). Homogeneous $Cp^*Rh(bpy)H_2O$ and monomers gave inferior performance, underscoring the importance of ordered, framework-anchored Rh sites for selective photocatalysis.

To elucidate the role of the Rh-induced electronic microenvironment in NADH regioselectivity, DFT calculations were performed on hydride transfer between Cp^*Rh sites and the NAD^+ pyridine ring (Figure S17). Adsorption energies indicated a thermodynamic preference for C-4 binding (−42.47 kJ mol^{-1}) over C-6 (−37.39) and C-2 (−41.31) sites (Table S7). Free energy profiles revealed a lower activation barrier for 1,4-NADH formation (15.57 kJ mol^{-1}) compared to 1,6-NADH (19.12) and 1,2-NADH (28.57) pathways (Figure 3e, Figure S18), consistent with experimental selectivity trends. In Rh-free HOF-2, broader H-transfer complexes favored non-selective pathways, particularly 1,6-NADH (22.54 kJ mol^{-1}), while 1,4-NADH formation was kinetically disfavored (47.83 kJ mol^{-1}) (Figure 3f, Figure S19-21). Minor routes such as 1,2-NADH proceeded via even higher barriers. These results demonstrate that the Rh incorporation enforces site-specific hydride delivery to the bioactive 1,4-NADH isomer.

Mechanistic Insights into Confinement-Regulated Energy and Mass Transport in HOF-2-Rh. To unravel the origins of the exceptional photocatalytic NADH regeneration efficiency in HOF-2-Rh, we investigate how confined microenvironments orchestrate sequential processes—exciton diffusion/dissociation, charge separation/transport, and proton conduction—that collectively govern NADH regeneration. [6,18,19]

Exciton Dynamics under Micropore Confinement. We employed femtosecond transient absorption spectroscopy (fs-TAS) to probe exciton dynamics in HOFs. Compared with a mixture of the HOF precursors (MTA and BPDA-Rh), spectral deconvolution of the fs-TAS signals of HOF-2-Rh revealed a distinct ground-state bleach (GSB) at 433 nm (F_2) (Figure 4b), in addition to the shared 379 nm (F_1) signal (Figure 4a,b), indicative of a well- defined energy level distribution arising from crystalline packing.[35-37] Such structural order suppresses energetic traps and promotes exciton diffusion by enabling efficient transport pathways within the lattice.[38] In contrast, the monomer mixture exhibited a broadened GSB band (Figure 4a), reflecting microscopic energy-level inhomogeneity and inefficient exciton relaxation caused by structural disorder. Notably, HOF-2 displayed even broader GSB features than HOF-2-Rh, underscoring the role of Cp^*Rh coordination in refining the lattice electronic structure to enhance exciton delocalization and dissociation. This role is further supported by the pronounced excited-state signals and rapid decay kinetics observed in the HOF-2—hallmarks of inefficient exciton delocalization and rapid annihilation (Figure S23). In contrast, excitons in HOF-2-Rh undergo rapid dissociation within confined micropores, where embedded Cp^*Rh sites facilitate this process by enhancing directional electronic conductivity. This interpretation is corroborated by the emergence of pronounced inhomogeneous broadening in the GSB of HOF-2-Rh under high excitation densities (Figure S24), accompanied by intensified excited-state signals and accelerated GSB decay (Figure 4d)—a combined spectroscopic signature of exciton annihilation when the Rh-mediated dissociation pathway becomes saturated. To further quantify the effect of confinement on migration behavior, we extracted the exciton diffusion length (L_t) in HOF-2-Rh by correlating bimolecular recombination rates with excitation fluence (Table S8).[30,39] The resulting L_t of 1.85 ± 0.03 nm agrees well with the channel dimensions determined by SCXRD (1.76–1.84 nm, Figure S1b) and cryo-TEM (1.87 nm, Figure 4g), providing direct structural evidence for a confinement-governed exciton diffusion regime.

Additional insights into exciton dynamics were obtained from biexponential kinetic fitting (Figure 4e), where τ_1 corresponds to ultrafast dissociation of high-density excitons or charge-transfer states, and τ_2 represents slower decay processes such as recombination, defect trapping, or long-range transport.[27,40] Compared to the monomers, HOF-2-Rh exhibited a shortened τ_1 (60.03 ps vs. 237.4 ps), indicating accelerated exciton dissociation and charge transfer facilitated via efficient capture at microporous interfaces. In parallel, its prolonged τ_2 (1521.7 ps vs. 1111.8 ps) reflects suppressed recombination and extended carrier lifetimes. Together, these kinetic and structural results support a confinement-governed exciton dissociation model, wherein photogenerated excitons in HOF-2-Rh undergo ultrashort-range diffusion before being captured at micropore interfaces. This behavior stands in sharp contrast to the long-range diffusion paradigm in conventional materials and highlights spatial restriction as a powerful design strategy for promoting charge separation. By mitigating diffusion losses, this architecture achieves efficient exciton dissociation, underpinning the high AQY in NADH photo-regeneration.

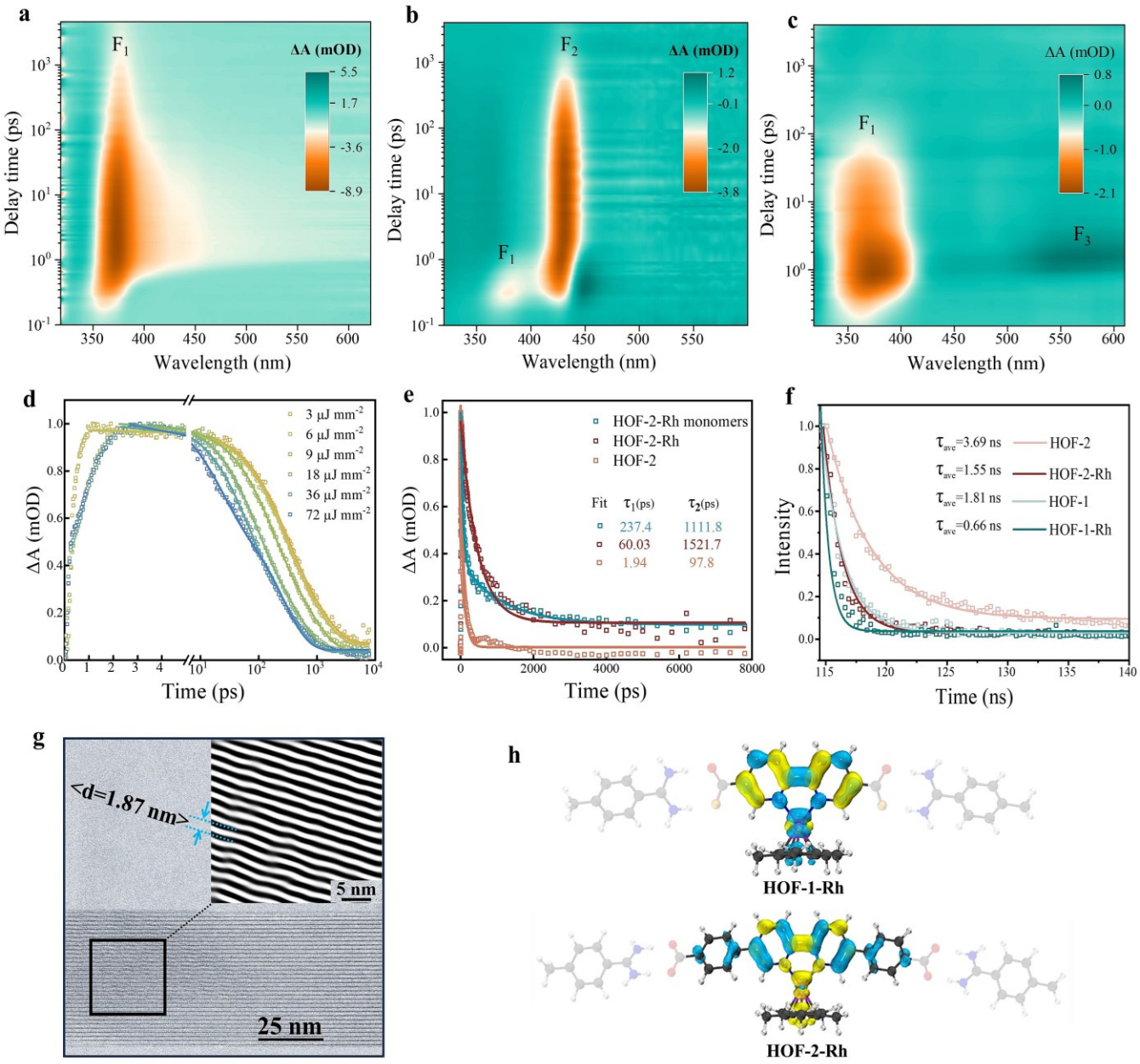

Figure 4. Femtosecond transient absorption contour plot of (a) HOF-2-Rh monomers (MTA/BPDA-Rh mixture), (b) HOF-2-Rh, and (c) HOF-2. (d) Kinetics of exciton absorption decay at various powers (excitation wavelength 400 nm). (e) Fs-TAS decay kinetics of HOF-2-Rh monomers, HOF-2-Rh, and HOF-2 at 375 nm, 433 nm, and 377 nm, respectively. (f) Fluorescence lifetimes of HOF-1, HOF-2, HOF-1-Rh, and HOF-2-Rh. (g) High-resolution TEM (HRTEM) images of HOF-2-Rh and the distinct one-dimensional channels with a uniform diameter of 1.87 nm can be observed. (h) Electron-hole distribution for the excited HOF-2-Rh and HOF-1-Rh (isovalue= ±0.002 e/Å^3). Blue area represents the hole, and yellow area represents the electron. The gray, blue, red and white balls represent C, N, O and H, respectively.

Rh-Induced Electronic Confinement in Carrier Separation and Transfer. While spatial confinement promotes exciton dissociation, efficient charge separation and transport are equally critical for minimizing recombination losses and ensure photocatalytic efficiency. Steady-state photoluminescence (PL) spectra revealed reduced emission intensity for HOF-2-Rh (quantum yield = 5.72%) compared with HOF-2 (quantum yield = 10.09%) (Figure S25), indicating suppressed radiative recombination upon Rh incorporation. Correspondingly, the shorter fluorescence lifetime of HOF-2-Rh (1.55 ns) relative to HOF-2 (3.69 ns) (Figure 4f) reflects accelerated depopulation of the excited state via electron extraction by Cp*Rh centers. Moreover, visible light-induced electron paramagnetic resonance (EPR) spectroscopy of HOF-2-Rh exhibited an enhanced signal at g = 2.0023 (Figure S26), providing direct evidence for the formation of stabilized charge-separated states through efficient photoinduced electron–hole separation. Together, these complementary spectroscopic results confirm that Cp*Rh functions as an intraframework electron acceptor, enabling efficient carrier separation by facilitating electron transfer from the excited organic backbone while suppressing recombination—thus creating an electronically favorable microenvironment for photocatalysis.

To elucidate the electronic factors governing carrier separation, we performed time-dependent density functional theory (TD-DFT) calculations to probe the excited-state electronic structure of HOF-2-Rh (Figure S27). Calculations at the DSD-PBEP86/def2-TZVP level revealed several key differences compared to HOF-1-Rh. HOF-2-Rh exhibited a lower $S_0 \rightarrow S_1$ transition energy (2.44 eV vs. 3.16 eV) and a larger oscillator strength (f = 0.556 vs. 0.356) (Table S10), indicating more efficient photoexcitation and a reduced conduction band minimum (–0.91 eV). Excited-state electron–hole analysis showed that HOF-2-Rh promotes charge separation, with a greater centroid distance between photogenerated holes and electrons (D = 0.92 Å vs. 0.66 Å) and reduced spatial overlap (S_r = 0.609 vs. 0.656). These features suggest weaker Coulombic attraction and suppressed recombination,[41,42] consistent with its lower exciton binding energy (E_b = 3.34 eV vs. 3.42 eV), implying that the excited-state electron is more easily dissociated and available for transfer. Structurally, the coplanar arrangement of phenyl units enhances π-conjugation and facilitates charge delocalization along the framework, while the precise positioning of Cp*Rh creates intraframework electron-accepting centers. This dual modulation establishes a cooperative micro-environment for efficient charge separation. Frontier orbital analyses further corroborate these findings: photoexcited holes localize mainly on the bipyridine moieties, while electrons concentrate at the Cp*Rh coordination sites (Figure 4h), confirming that Cp*Rh generates a confined electronic environment that suppresses recombination losses and accelerates electron transfer. Having established the role of Cp*Rh coordination in carrier separation, we next examined its impact on intraframework electron transport in HOF-2-Rh. Transient photocurrent measurements showed stronger photoresponses for HOF-2 than HOF-1 (Figure 5a), consistent with more efficient carrier separation, but Rh incorporation attenuated the signal–likely due to the high work function of Cp*Rh (~4.98 eV),[43] which hinders electron injection into the electrode and favors charge retention within the framework. Electrochemical impedance spectroscopy (EIS) confirmed enhanced internal conductivity, with HOF-2-Rh displaying a smaller Nyquist semi- circle (Figure 5b). This disparity between external photocurrent and internal transport indicates that Cp*Rh promotes internal electron delivery for catalysis. Femtosecond transient absorption spectroscopy (fs-TAS) revealed a temporally synchronized anti-correlation between F_1 decay and F_2 rise, signifying rapid electron transfer from the organic backbone to Rh centers. Kinetic fitting yielded an electron transfer time constant of 0.843 ps (Figure 5c, S28). In contrast, HOF-2 lacked the F_2 feature and exhibited a broadened F_1 profile with an additional excited-state absorption (F_3) (Figure S29), indicative of charge localization and enhanced non-radiative decay in the absence of electron acceptors. The emergence and ultrafast dynamics of F_2 in HOF-2-Rh thus provide direct spectroscopic evidence that Cp*Rh imposes kinetic control over electron flow via a confined electronic microenvironment–crucial for sustaining carrier separation and enabling directional electron transfer.

Hydrogen Bond Interaction-Confined Proton Conduction. In addition to electron transfer, efficient proton transport is critical for completing the NAD^+ reduction cycle.[44] The internal hydrogen-bond network in HOF-2-Rh imposes structural constraints and dynamically regulates hydrogen bonding to facilitate proton conduction. Impedance measurements showed that proton conductivity increased from 4.68×10^{-5} to 2.83×10^{-3} S cm^{-1} as relative humidity (RH) increased from 65% to 95% at 30 °C (Figure S30), and further reached 1.26×10^{-2} S cm^{-1} at 80 °C under 95% RH–a 4.5-fold enhancement (Figure 5d)–highlighting the role of water molecule in establishing conduction pathways and the thermally induced dynamic restructuring of the hydrogen-bond network. The activation energy (E_a = 0.46 eV) falls within the range of the Grotthuss mechanism,[45] indicating hydrogen-bond-mediated proton hopping within confined channels.

Molecular dynamics (MD) simulations revealed ordered water clusters forming after 100 ns (Figure 5e), serving as the structural backbone of the conduction network. Bader charge

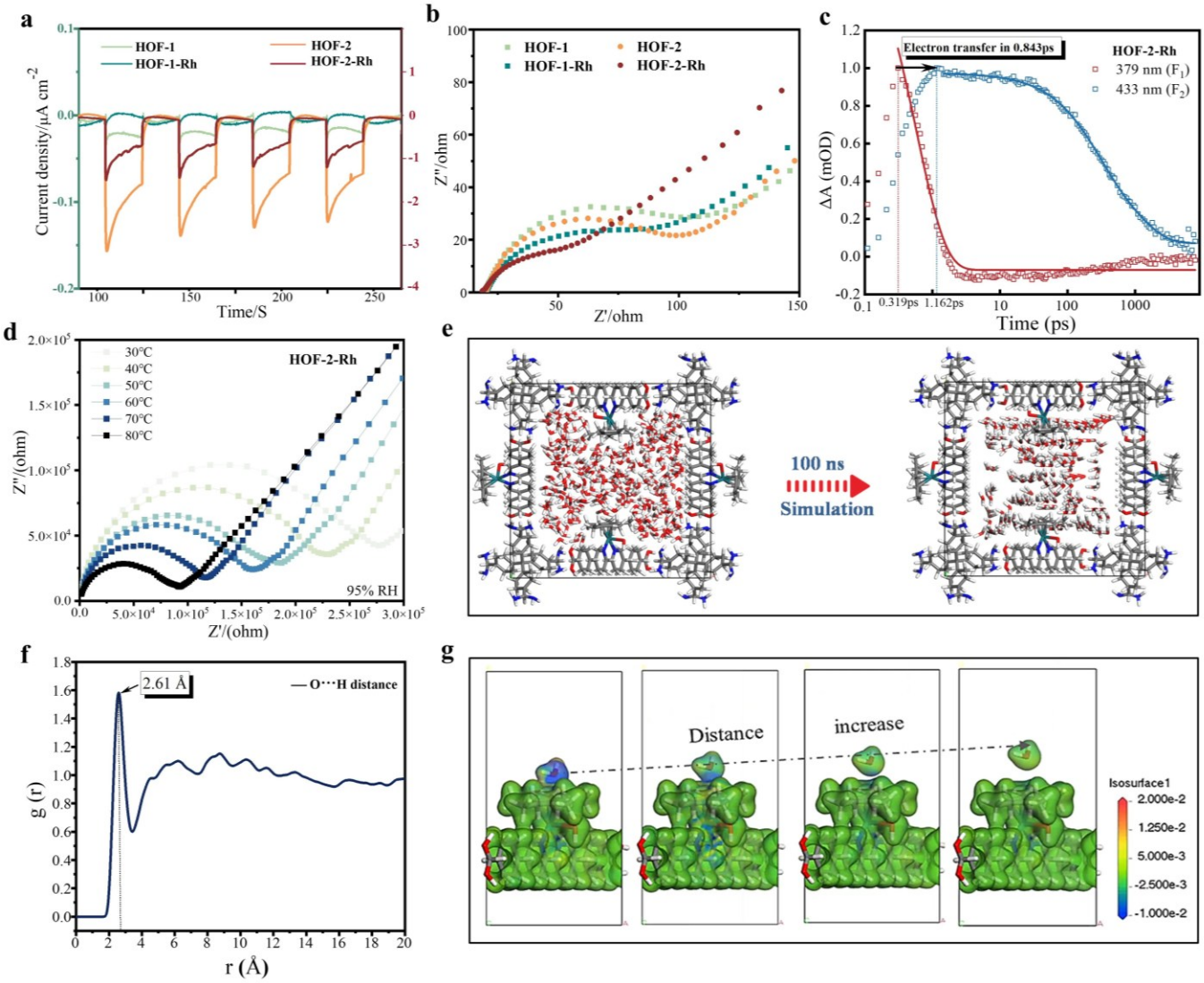

Figure 5. (a) Photocurrent response and (b) electrochemical impedance spectroscopy of HOFs. (c) Fitting of the signal decay kinetics of F_1 peak (379 nm) and F_2 peak (433 nm) of HOF-2-Rh. (d) The effect of temperature on the proton conductivity of HOF-2-Rh. (e) Structural characteristic of water molecules confined within HOF-2-Rh sub-nanocrystals. (f) Radial distribution function between water oxygen atoms and framework hydrogen atoms. (g)The contour map of differential charge density of the water molecules upon approaching the polarity sites in HOF walls.

analysis indicated strong polarization of water molecules near polar framework groups (Figure 5g), enabling dynamic hydrogen–bond reorganization essential for intermolecular proton hopping. Radial distribution function (RDF) showed sharp maxima at sub-3 Å O–H distances (Figure 5f), consistent with extensive hydrogen bonding between confined water and the framework, yielding directional hydrogen-bond chains that act as proton wires between water oxygen atoms and framework hydrogen atoms, indicative of extensive formation of stable hydrogen bonds between confined water and the framework.[46] This short-range interaction reflects a structured water network templated by the pore wall, enabling the formation of directional hydrogen-bond chains that act as proton wires. Such spatially organized interactions are essential for sustaining Grotthuss-type proton hopping by lowering activation barriers and promoting intermolecular proton exchange.[45] Mean square displacement (MSD) analysis revealed a water diffusion coefficient of 0.02069 $Å^2$ ps^{-1} (Figure S31)—an order of magnitude lower than bulk water (~0.2–0.3 $Å^2$ ps^{-1})[47]—indicating that geometric confinement and polarization

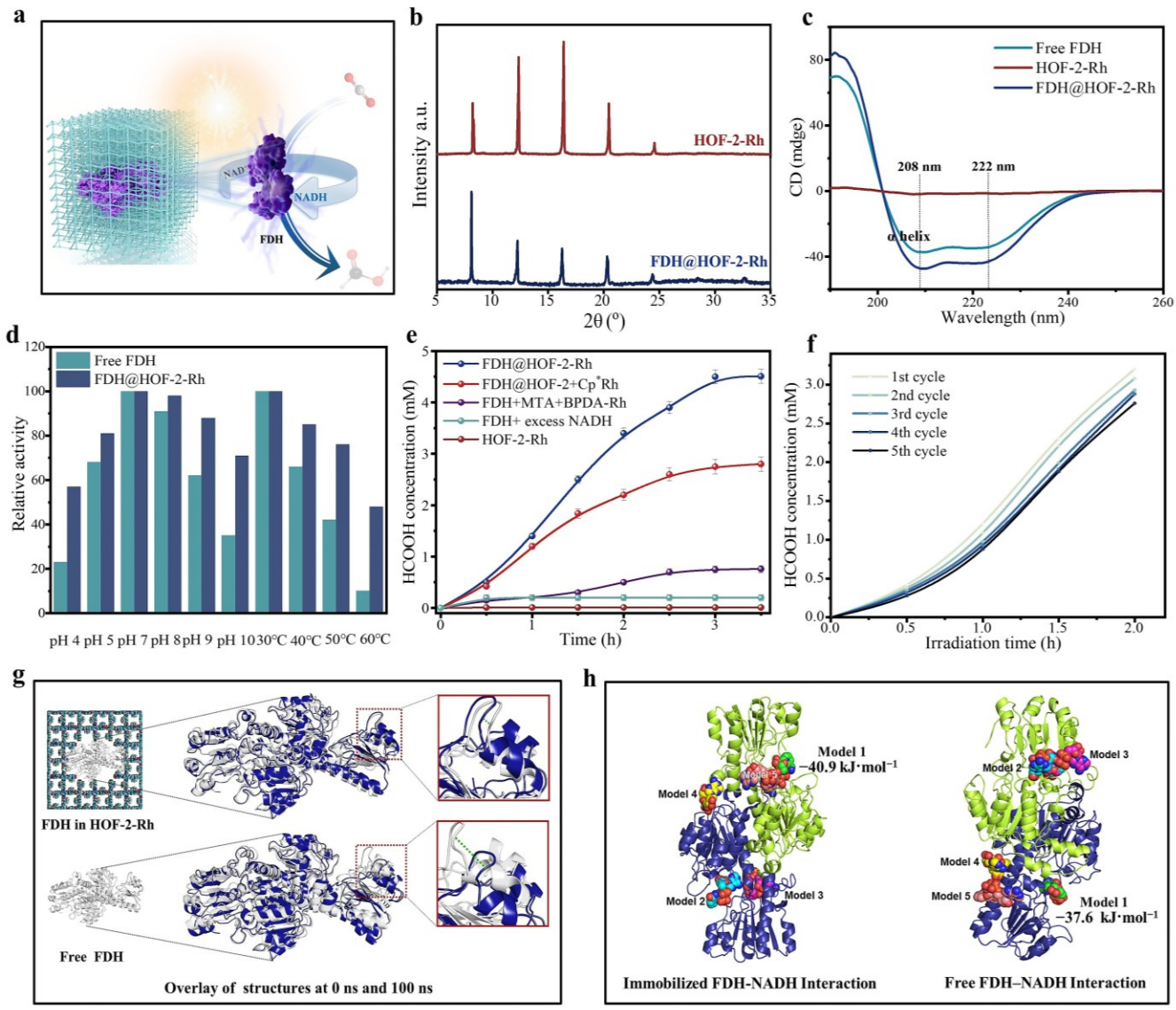

Figure 6. (a) Photoenzymatic system for CO_2 reduction to formate based on a facile one-pot co-precipitation strategy. (b) XRD and (c) CD of HOF-2-Rh and FDH@HOF-2-Rh, respectively. (d) The stability of free FDH and immobilized FDH in HOF after 1 hour treatment in different temperature and pH. (e) Kinetics of photoenzymatic production of formate over different catalysts in the presence of NAD^+ and CO_2 under 420 nm illumination. (f) Reusability of FDH@HOF-2-Rh for photoenzymatic production of formic acid. (g) The overlay alignment of the initial (gray) and simulated (100 ns, blue) structures of immobilized FDH and free FDH. (h) Conformations of the optimal binding modes of NADH to free FDH or immobilized FDH in HOF-2-Rh and their affinity energies.

suppress random diffusion while favoring structured proton transport. Together, these results show that the natural hydrogen-bonding architecture differ from traditional frameworks templates ordered, directional proton pathways crucial for sustaining Grotthuss-type conduction and enabling efficient NADH regeneration (Figure S32). Overall, the ordered architecture of HOF-2-Rh enables exceptional spatiotemporal confinement of energy and mass, orchestrating the efficient excitons dissociation, electron transfer, and proton conduction (Figure S34). Spatial confinement restricts exciton diffusion,

facilitating rapid interfacial charge separation, while atomically dispersed Cp^*Rh centers (Figure S33) serve as localized electron sinks, enabling ultrafast, directional electron transfer to the NAD^+ pyridine ring. Simultaneously, the intrinsic hydrogen-bond network establishes low-energy proton conduction pathways, thereby supporting efficient coupled proton-electron transport. In contrast to conventional MOFs and COFs, the dynamic and tunable hydrogen-bond network in HOF provides unparalleled flexibility in modulating spatial confinement, electronic modulation, and hydrogen-bond interactions. This unique feature makes HOFs an effective platform for synergistically coupling photocatalysis with enzymatic catalysis.

Construction of Photoenzymatic Systems for CO_2-to-Formate Reduction. An integrated photoenzymatic cascade, coupling light-driven NADH regeneration with enzymatic CO_2 reduction, was constructed to evaluate the efficiency of CO_2 conversion to formate. Leveraging the proven capability of HOF-2-Rh for photorecycling 1,4-NADH, formate dehydrogenase (FDH) from *Candida boidinii* was immobilized via a one-pot co-precipitation strategy, yielding the hybrid biocatalyst FDH@HOF-2-Rh (Figure 6a). SEM and PXRD confirmed that enzyme encapsulation caused no detectable morphological or crystallographic changes, while EDS, FTIR, and circular dichroism (CD) spectroscopy verified in situ incorporation of FDH and preservation of its α-helical structure (Figure 6b, c; Figure S35, 36). Confocal laser scanning microscopy (CLSM) imaging of fluorescently labeled FDH demonstrated homogeneous distribution throughout the framework (Figure S37), and adsorption/zeta potential analyses excluded post-synthetic infiltration (Table S13, Figure S38). Enzyme loading analysis revealed complete incorporation over 0.25–1.5 mg mL^{-1}, achieving high loadings (13.7–51.4%) and specific activities (1314–4936 U g^{-1}), surpassing conventional protein@MOF systems (<15%) and other bottom-up biohybrid frameworks (Table S11, 12). This enhancement is attributed to the unobstructed protein dispersion via in situ immobilization, which avoids steric and diffusional constraints typically associated with post-loading in traditional MOF and COF.[48] FDH@HOF-2-Rh showed minimal leaching (< 2.3%) across pH 5–9, in contrast to benchmark FDH@HOF101 (>95% leaching under alkaline conditions; Table S14). Fluorescein diffusion confirmed that internal microchannels remained accessible post-encapsulation (Figure S39), preserving porosity essential for triphasic catalysis. Under 420 nm visible light irradiation, FDH@ HOF-2-Rh produced 4.53 mM formate in 3 h with a specific activity of 3020 μmol g^{-1} h^{-1} (Figure 6e), surpassing all reported aqueous light-driven systems, encompassing both purely photocatalytic and photoenzymatic platforms (Table S15). The catalytic specificity of FDH ensures that formate is the sole product. This performance stems from the integration of efficient NADH regeneration, high FDH loading, and preserved transport channels. Control experiments with physically mixed or non-hierarchical assemblies showed reduced activity (Figure 6e), underscoring the role of ordered architecture in maintaining enzymatic proximity. The system retained 86.3% activity over five CO_2 reduction cycles (Figure 6f) and exhibited superior pH and thermal stability relative to free FDH (Figure 6d), demonstrating its robustness and practical potential.

All-atom molecular dynamics (MD) simulations[49] were performed to assess how the nanoscale architecture of HOF-2-Rh stabilizes FDH and facilitates NADH diffusion. Over a 100 ns trajectory, free FDH exhibited substantial structural fluctuations, whereas the encapsulated enzyme largely retained its native fold (Figure 6g), consistent with reduced backbone RMSD (root-mean-square deviations) and lower residue-level RMSF (root-mean-square fluctuations) (Figure S40i, ii). These results indicate that the framework acts as a conformational scaffold to preserve enzymatic structure. Compared to free FDH, the immobilized enzyme formed denser hydrogen-bond networks with NADH (mean count: 9.1 vs. 5.2) and a larger contact area (11.44 vs. 10.69 nm^2) (Figure S40iii, iv), yielding a more stable binding interface. Time-resolved interaction energy analyses revealed persistent FDH–NADH complex formation within the HOF-2-Rh matrix (Figure S41), with enhanced binding affinity reflected in a more favorable binding energy (–40.9 vs. –37.6 kJ mol^{-1}) (Figure 6h, Table S16). These structural and interactional benefits translated into ~120% relative activity compared free FDH at identical protein concentrations, alongside a lower K_m for sodium formate (0.16 vs. 0.19 mM), indicating improved substrate affinity. Consequently, the hydrogen-bonded scaffold plays a dual role in stabilizing FDH and strengthening cofactor interaction, facilitating an optimized microenvironment for enhanced CO_2-to-formate reduction.

■ CONCLUSIONS

In summary, we developed an efficient HOF-based photoenzymatic platform for CO_2-to-formate conversion in water by simple one-pot in situ co-assembly of photoactive ligands, Rh-based electron relays, and formate dehydrogenase (FDH). The optimal photocatalyst, HOF-2-Rh@FDH, delivers 99.8% efficiency for photocatalytic NADH regeneration and a formate production rate of 3020 μmol g^{-1} h^{-1}, both of which represent record values for light-driven aqueous systems reported to date. Upon visible-light irradiation, spatial confinement within HOF-2-Rh suppresses long-range exciton diffusion and promotes rapid interfacial charge separation, while atomically dispersed Cp^*Rh centers on the ligands act as localized electron sinks, enabling ultrafast, directional electron transfer to NAD^+. Concurrently, the intrinsic hydrogen-bond networks provide low-barrier pathways for proton conduction

to NAD^+, and enhance enzyme-NADH interactions. These confined microenvironments synergistically coordinate efficient excitons dissociation, electron transfer, proton conduction, thereby achieving exceptional spatiotemporal funneling of energy and mass transport into the formate-forming pathway. The insights gained from this work deepen the understanding of the transport behavior of photogenerated species and underscore the pivotal role of HOFs in the rational design of advanced photoenzymatic catalytic systems.

■ ASSOCIATED CONTENT

Supporting Information.

The Supporting Information is available free of charge via the Internet at http://pubs.acs.org. Chemicals and methods, additional characterization of HOFs, photocatalytic and photoenzymatic tests, fs-TAS, DFT calculations, and MD simulations.

Accession Codes

The CCDC numbers 2308912, 2308913, 2382547, and 2382548 correspond to four HOF materials. These data can be obtained via www.ccdc.cam.ac.uk/data_request/cif.

■ AUTHOR INFORMATION

***Xu Zhang – School of Chemistry and Chemical Engineering,** Huaiyin Normal University, Jiangsu Engineering Laboratory for Environment Functional Materials, Jiangsu Collaborative Innovation Center of Regional Modern Agriculture & Environmental Protection, Huaian, Jiangsu 223300, China; 0000-0001-9114-1842; Email: zhangxu@hytc.edu.cn

***Jian Zhang** – The Molecular Foundry, Lawrence Berkeley National Laboratory, Berkeley, California 94720, United States; orcid.org/0000-0003-0274-0814; Email: jianzhang@lbl.gov

Authors

†Jiaxing Xu – Jiangsu Key Laboratory for Biomass-Based Energy and Enzyme Technology, School of Chemistry and Chemical Engineering, Huaiyin Normal University, Huaian 223300, China; orcid.org/0000-0002-9112-5161; Email: xujiaxing@hytc.edu.cn;

†Xiang Zhang – Jiangsu Key Laboratory for Biomass-Based Energy and Enzyme Technology, School of Chemistry and Chemical Engineering, Huaiyin Normal University, Huaian 223300, China;

†Lijuan Ma – Jiangsu Key Laboratory for Biomass-Based Energy and Enzyme Technology, School of Chemistry and Chemical Engineering, Huaiyin Normal University, Huaian 223300, China;

†Tao Wu – Jiangsu Key Laboratory for Biomass-Based Energy and Enzyme Technology, School of Chemistry and Chemical Engineering, Huaiyin Normal University, Huaian 223300, China; orcid.org/0000-0003-0536-7381;

†Hui Wang – Jiangsu Key Laboratory for Biomass-Based Energy and Enzyme Technology, School of Chemistry and Chemical Engineering, Huaiyin Normal University, Huaian 223300, China;

†Yuanfang Deng – Jiangsu Key Laboratory for Biomass-Based Energy and Enzyme Technology, School of Chemistry and Chemical Engineering, Huaiyin Normal University, Huaian 223300, China; orcid.org/0000-0003-0520-4144;

†Jun Xia – Jiangsu Key Laboratory for Biomass-Based Energy and Enzyme Technology, School of Chemistry and Chemical Engineering, Huaiyin Normal University, Huaian 223300, China; orcid.org/0000-0001-6212-0831

†Zhongyang Qiu – Jiangsu Key Laboratory for Biomass-Based Energy and Enzyme Technology, School of Chemistry and Chemical Engineering, Huaiyin Normal University, Huaian 223300, China;

†Kai Sun – Jiangsu Key Laboratory for Biomass-Based Energy and Enzyme Technology, School of Chemistry and Chemical Engineering, Huaiyin Normal University, Huaian 223300, China;

†Aiyong He – Jiangsu Key Laboratory for Biomass-Based Energy and Enzyme Technology, School of Chemistry and Chemical Engineering, Huaiyin Normal University, Huaian 223300, China;

‖Banglin Chen – Fujian Provincial Key Laboratory of Polymer Materials, College of Chemistry and Materials, Fujian Normal University, Fuzhou 350007, China; Key Laboratory of the Ministry of Education for Advanced Catalysis Materials, College of Chemistry and Materials Science, Zhejiang Normal University, Jinhua 321004, China. orcid.org/0000-0001-8707-8115.

Author Contributions

§Jiaxing Xu and Xiang Zhang are equally contributing authors.

Notes

The authors declare no competing financial interest.

■ ACKNOWLEDGMENT

This work was supported by the Joint Funds of the National Natural Science Foundation of China (Grant No. U22A20426), and National Natural Science Foundation of China (22275064 and 22308115). We also thank the staff of BL17B1 beamline at the National Facility for Protein Science (NFPS) of the Shanghai Synchrotron Radiation Facility (SSRF), Shanghai, People's Republic of China, for assistance during data collection. The work conducted at the Molecular Foundry, Lawrence Berkeley National Laboratory, was supported by the Office of Science, Office of Basic Energy Sciences, of the U.S. Department of Energy under Contract No. DE-AC02-05CH11231.

■ REFERENCES

(1) Vogt, E.T.C.; Weckhuysen, B.M. The refinery of the future. *Nat.* **2024**, 629, 295–306.

(2) Wei, D.; Sang, R.; Sponholz, P.; Junge, H.; Beller, M. Reversible hydrogenation of carbon dioxide to formic acid using a Mn-pincer complex in the presence of lysine. *Nat. Energy* **2022**, 7, 438–447.

(3) Tan, T. H.; Xie, B.; Ng, Y. H.; Abdullah, S. F. B.; Tang, H. Y. M.; Bedford, N.; Taylor, R. A.; Aguey-Zinsou, K.-F.; Amal, R.; Scott, J. Unlocking the potential of the formate pathway in the photo-assisted Sabatier reaction. *Nat. Catal.* **2020**, 3, 1034–1043.

(4) Guo, Z.; Chen, G.; Cometto, C.; Ma, B.; Zhao, H.; Groizard, T.; Chen, L.; Fan, H.; Man, W.-L.; Yiu, S.-M.; Lau, K.-C.; Lau, T.-C.; Robert, M. Selectivity control of CO versus HCOO− production in the visible-light-driven catalytic reduction of CO_2 with two cooperative metal sites. *Nat. Catal.* **2019**, 2, 801–808.

(5) Jiang, Z.; Xu, X.; Ma, Y.; Cho, H. S.; Ding, D.; Wang, C.; Wu, J.; Oleynikov, P.; Jia, M.; Cheng, J.; Zhou, Y.; Terasaki, O.; Peng, T.; Zan, L.; Deng, H. Filling metal–organic framework mesopores with TiO_2 for CO_2 photoreduction. *Nat.* **2020**, 586, 549–554.

(6) Hao, Y.-C.; Chen, L.-W.; Li, J.; Guo, Y.; Su, X.; Shu, M.; Zhang, Q.; Gao, W.-Y.; Li, S.; Yu, Z.-L.; Gu, L.; Feng, X.; Yin, A.-X.; Si, R.; Zhang, Y.-W.; Wang, B.; Yan, C.-H. Metal-organic framework membranes with single-atomic centers for photocatalytic CO_2 and O_2 reduction. *Nat. Commun.* **2021**, 12, 2682.

(7) Yao, L.; Pütz, A. M.; Vignolo-González, H.; Lotsch, B. V. Covalent organic frameworks as single-site photocatalysts for solar-to-fuel conversion. *J. Am. Chem. Soc.* **2024**, 146, 9479–9492.

(8) Hirani, Z.; Schweitzer, N. M.; Vitaku, E.; Dichtel, W. R. A phenazine-based two-dimensional covalent organic framework for photochemical CO_2 reduction with increased selectivity for two-carbon products. *Angew. Chem., Int. Ed.* **2025**, 64, e202502799.

(9) Gong, Y.-N.; Mei, J.-H.; Shi, W.-J.; Liu, J.-W.; Zhong, D.-C.; Lu, T.-B. Boosting CO_2 photoreduction to formate or CO with high selectivity over a covalent organic framework covalently anchored on graphene oxide. *Angew. Chem., Int. Ed.* **2024**, 63, e202318735.

(10) Cai, Z.; Liu, H.; Dai, J.; Li, B.; Yang, L.; Wang, J.; Zhu, H. Sunlight-driven simultaneous CO_2 reduction and water oxidation using indium-organic framework heterostructures. *Nat. Commun.* **2025**, 16, 2601.

(11) Tamaki, Y.; Morimoto, T.; Koike, K.; Ishitani, O. Photocatalytic CO_2 reduction with high turnover frequency and selectivity of formic acid formation using Ru(II) multinuclear complexes. *Proc. Natl. Acad. Sci. U.S.A.* **2012**, 109, 15673–15678.

(12) Xie, W.; Xu, J.; Idros, U. M.; Katsuhira, J.; Fuki, M.; Hayashi, M.; Yamanaka, M.; Kobori, Y.; Matsubara, R. Metal-free reduction of CO_2 to formate using a photochemical organ hydride-catalyst recycling strategy. *Nat. Chem.* **2023**, 15, 794–802.

(13) Lewis, N. S. Developing a scalable artificial photosynthesis technology through nanomaterials by design. *Nat. Nanotechnol.* **2016**, 11, 1010–1019.

(14) Fang, S.; Rahaman, M.; Bharti, J.; Reisner, E.; Robert, M.; Ozin, G. A.; Hu, Y. H. Photocatalytic CO_2 reduction. *Nat. Rev. Methods Primers* **2023**, 3, 61.

(15) Gao, F.; Liu, G.; Chen, A.; Hu, Y.; Wang, H.; Pan, J.; Feng, J.; Zhang, H.; Wang, Y.; Min, Y.; Gao, C.; Xiong, Y. Artificial photosynthetic cells with biotic-abiotic hybrid energy modules for customized CO_2 conversion. *Nat. Commun.* **2023**, 14, 6783.

(16) Chen, Q.; Wang, Y.; Luo, G. Photoenzymatic CO_2 reduction dominated by collaborative matching of linkage and linker in covalent organic frameworks. *J. Am. Chem. Soc.* **2024**, 146, 586–598.

(17) Lin, G.; Zhang, Y.; Hua, Y.; Zhang, C.; Jia, C.; Ju, D.; Yu, C.; Li, P.; Liu, J. Bioinspired metalation of the metal-organic framework MIL-125-NH_2 for photocatalytic NADH regeneration and gas-liquid-solid three-phase enzymatic CO_2 reduction. *Angew. Chem., Int. Ed.* **2022**, 61, e202206283.

(18) Tong, L.; Gong Z.; Wang, Y.; Luo, J.; Huang, S.; Gao, R.; Chen, G.; Ouyang, G. Atomically precise regulation of the N-heterocyclic microenvironment in triazine covalent organic frameworks for coenzyme photocatalytic regeneration. *J. Am. Chem. Soc.* **2024**, 146 21025-21033

(19) Chen, Q.; Wang, Y.; Luo, G. Photoenzymatic CO_2 reduction dominated by collaborative matching of linkage and linker in covalent organic frameworks. *J. Am. Chem. Soc.* **2024**, 146, 586–598.

(20) Lin, G.; Zhang, Y.; Hua, Y.; Zhang, C.; Jia, C.; Ju, D.; Yu, C.; Li, P.; Liu, J. Bioinspired metalation of the metal-organic framework MIL-125-NH_2 for photocatalytic NADH regeneration and gas-liquid-solid three-phase enzymatic CO_2 reduction. *Angew. Chem., Int. Ed.* **2022**, 61, e202206283.

(21) Tong, L.; Gong Z.; Wang, Y.; Luo, J.; Huang, S.; Gao, R.; Chen, G.; Ouyang, G. Atomically precise regulation of the N-heterocyclic microenvironment in triazine covalent organic frameworks for coenzyme photocatalytic regeneration. *J. Am. Chem. Soc.* **2024**, 146 21025–21033

(22) Tang, J.; Lei, Y.; Tang, Q.; Lei, S.; Qi, Q.-Y.; Li, Z.-T.; Tian, J. Integration of multiple enzymes within hydrogen-bonded organic frameworks for efficient cascade photocatalytic CO_2-to-methanol conversion in water. *Angew. Chem., Int. Ed.* **2025**, 64, e202516599.

(23) Chen, G.; Huang, S.; Ma, X.; He, R.; Ouyang, G. Encapsulating and stabilizing enzymes using hydrogen-bonded organic frameworks. *Nat. Protoc.* **2023**, 18, 2032–2050.

(24) Lin, R.-B.; Chen, B. Hydrogen-bonded organic frameworks: Chemistry and functions. *Chem.* **2022**, 8, 2114–2135.

(25) Wang, B.; Lin, R.-B.; Zhang, Z.; Xiang, S.; Chen, B. Hydrogen-bonded organic frameworks as a tunable platform for functional materials. *J. Am. Chem. Soc.* **2020**, 142, 14399–14416.

(26) Bernardina, S. D.; Paineau, E.; Brubach, J. -B.; Judeinstein, P.; Rouzière, S. Water in carbon nanotubes: the peculiar hydrogen bond network revealed by infrared spectroscopy. *J. Am. Chem. Soc.* **2016**, 138, 10437–10443.

(27) Zhou, Q.; Guo, Y.; Zhu, Y. Photocatalytic sacrificial H_2 evolution dominated by micropore-confined exciton transfer in hydrogen-bonded organic frameworks. *Nat. Catal.* **2023**, 6, 574–584.

(28) Wang, H.; Liu, W.; He, X.; Zhang, P.; Zhang, X.; Xie, Y. An excitonic perspective on low-dimensional semiconductors for photocatalysis. *J. Am. Chem. Soc.* **2020**, 142, 14007–14022.

(29) Sun, C.; Wu, Z.; Hu, Z.; Xiao, J.; Zhao, W.; Li, H.-W.; Li, Q.-Y.; Tsang, S.-W.; Xu, Y.-X.; Zhang, K.; Yip, H.-L.; Hou, J.; Huang, F.; Cao, Y. Interface design for high-efficiency non-fullerene polymer solar cells. *Energy Environ. Sci.* **2017**, 10, 1784–1791.

(30) Mikhnenko, O. V.; Blom, P. W. M.; Nguyen, T. Q. Exciton diffusion in organic semiconductors. *Energy Environ. Sci.* **2015**, 8, 1867–1888.

(31) Funke, H.; Scheinost, A. C.; Chukalina, M. Wavelet analysis of extended X-ray absorption fine structure data. *Phys. Rev. B* **2005**, 71, 094110.

(32) Veine, D. M.; Arscott, L. D.; Williams, C. H. Redox potentials for yeast, Escherichia coli and human glutathione reductase relative to the NAD^+/NADH redox couple: enzyme forms active in catalysis. *Biochem.* **1998**, 37, 15575–15582.

(33) Liu, S.; Shi, J.; Jia, J.; Yang, Y.; Zhang, S.; Yang, D.; Chen, Y.; Li, S.; Jiang, Z. Metal-free light-driven 1,4-NADH regeneration system from nitrogen and sulfur codoped carbon dots. *ACS Catal.* **2023**, 13, 14233–14240.

(34) Saba, T.; Li, J.; Burnett, J. W. H.; Howe, R. F.; Kechagiopoulos, P. N.; Wang, X. NADH regeneration: a case study of Pt-catalyzed NAD^+ reduction with H_2. *ACS Catal.* **2021**, 11, 283–289.

(35) Flanders, N. C.; Kirschner, M. S.; Kim, P.; Fauvell, T. J.; Evans, A. M.; Helweh, W.; Spencer, A. P.; Schaller, R. D.; Dichtel, W. R.; Chen, L. X. Large exciton diffusion coefficients in two-dimensional covalent organic frameworks with different domain sizes revealed by ultrafast exciton dynamics. *J. Am. Chem. Soc.* **2020**, 142, 14957–14965.

(36) Chandrabose, S.; Pandey, L.; Holmes, R. J.; Forrest, S. R.; Lunt, R. R. High exciton diffusion coefficients in fused ring electron acceptor films. *J. Am. Chem. Soc.* **2019**, 141, 6922–6929.

(37) Mahato, P.; Monguzzi, A.; Yanai, N.; Yamada, T.; Kimizuka, N. Fast and long-range triplet exciton diffusion in metal–organic frameworks for photon up conversion at ultralow excitation power. *Nat. Mater.* **2015**, 14, 924–930.

(38) Müller, K.; Schellhammer, K. S.; Gräßler, N.; Debnath, B.; Liu, F.; Krupskaya, Y.; Leo, K.; Knupfer, M.; Ortmann, F. Directed exciton transport highways in organic semiconductors. *Nat. Commun.* **2023**, 14, 5599.

(39) Jin, X.-H.; Price, M. B.; Finnegan, J. R.; Boott, C. E.; Richter, J.M.; Rao, A.; Menke, S. M.; Friend, R.H.; Whittell, G.R. Manners, I. Long-range exciton transport in conjugated polymer nanofibers prepared by seeded growth. *Science* **2018**, 360, 897–900.

(40) Liu, M.; Liu, J.; Li, J.; Zhao, Z.; Zhou, K.; Li, Y.; He, P.; Wu, J.; Bao, Z.; Yang, Q.; Yang, Y.; Ren, Q.; Zhang, Z. Blending aryl ketone in covalent organic frameworks to promote photoinduced electron transfer. *J. Am. Chem. Soc.* **2023**, 145, 9198–9206.

(41) Passarelli, J. V.; Mauck, C. M.; Winslow, S. W.; Perkinson, C. F.; Bard, J. C.; Sai, H.; Narayanan, A.; Fairfield, D. J.; Hendricks, M. P.; Tisdale, W. A.; Stupp, S. I. Tunable exciton binding energy in 2D hybrid layered perovskites through donor–acceptor interactions within the organic layer. *Nat. Chem.* **2020**, 12, 672–682.

(42) Shao, Y.; Lu, T.; Li, M.; Lu, W. Theoretical exploration of diverse electron-deficient core and terminal groups in A–DA′D–A type non-fullerene acceptors for organic solar cells. *New J. Chem.* **2022**, 46, 3370–3382.

(43) Balduf, T.; Blakemore, J. D.; Caricato, M. Computational insights into the influence of ligands on hydrogen generation with [Cp^*Rh] hydrides. *J. Phys. Chem. A* **2023,** 127, 6020–6031.

(44) Saura, P.; Kaila, V. R. I. Energetics and dynamics of proton-coupled electron transfer in the NADH/FMN site of respiratory complex. *J. Am. Chem. Soc.* **2019**, 141, 14, 5710–5719

(45) Feng, X.; Zang, Q.; Feng, X.; Lv, B.; Yu, H.; Sun, T.; Yuan, Z.; Liu, J.; Yang, Y.; Zhang, F. Enhanced solar-to-hydrogen conversion and hydrogen isotope separation through interfacial hydrogen-bond engineering and homolytic O–H cleavage on multianionic sulfides in large-scale floating nanocomposites. *ACS Catal.* **2024**, 14, 9077–9092.

(46) Terban, M. W.; Billinge, S. J. L. Structural analysis of molecular materials using the pair distribution function. *Chem. Rev.* **2022,** 122, 1208–1272.

(47) Chakraborty, S.; Kumar, H.; Dasgupta, C.; Maiti, P. K. Confined water: structure, dynamics, and thermodynamics. *Acc. Chem. Res.* **2017**, 50, 2139–2146.

(48) Liang, W.; Wied, P.; Carraro, F.; Sumby, C. J.; Nidetzky, B.; Tsung, C.-K.; Falcaro, P.; Doonan, C. J. Metal–organic framework-based enzyme biocomposites. *Chem. Rev.* **2021**, 121, 1077–1129.

(49) Hess, B.; Kutzner, C.; van der Spoel, D.; Lindahl, E. GROMACS 4: algorithms for highly efficient, load-balanced, and scalable molecular simulation. *J. Chem. Theory Comput.* **2008**, 4, 435–447.

TOC Graphic